The PVD neuron has male-specific structure and mating function in *C. elegans*

Yael Iosilevskii[1], David H. Hall[2], Menachem Katz[1] and Benjamin Podbilewicz[1,#]

[1]Department of Biology, Technion- Israel Institute of Technology, Haifa 32000, Israel
[2]Department of Neuroscience, Albert Einstein College of Medicine, 1300 Morris Park Avenue, Bronx, NY 10461, USA

[#]Correspondence should be addressed to B.P. (podbilew@technion.ac.il).

Highlights:

- The sensory neuron PVD undergoes sexually dimorphic morphogenesis upon adulthood
- Male PVD extends dendritic arborization into the copulatory tail rays
- Male PVD follows unique SAX-7 distribution within a sex-shared patterning mechanism
- PVD has a sex-specific role during *C. elegans* male mating behavior

Significance statement

Neurons form intricate shapes and networks, which may display sexual differences. Pinpointing these changes at the single cell level, however, is challenging. In *C. elegans*, the PVD neuron is a powerful model for stereotypical neuron shaping, yet most studies concern only one of the two sexes. Our research focuses on the understudied male animal, where we show how a sex-shared patterning complex is able to form an adult-stage extension of the complex PVD dendrite into the male copulatory tail organ. We further find that PVD has a novel role in the male adult-specific mating behavior. PVD thus presents a unique example of a single highly arborized neuron showing sexually dimorphic behavioral function and structure.

Abstract

Neurons display unique shapes and establish intricate networks, which may differ between sexes. In complex organisms, studying sex differences in structure and function of individual neurons is difficult. The nematode *Caenorhabditis elegans* hermaphrodites and males present an exceptional model for studying neuronal morphogenesis in a simple, sexually-dimorphic system. We focus on the polymodal sensory bilateral neuron pair PVD, which forms a complex but stereotypic dendritic tree composed of multiple subunits that resemble candelabra. PVD is well studied in hermaphrodites, but not in males. We show here that during larval development, male PVDs extend a similar architecture to the hermaphrodite utilizing the sexually-shared Menorin patterning mechanism. In early adulthood, however, male PVD develops a unique extension into the copulatory tail structure. This sexually-dimorphic arborization is absent in mutant backgrounds which perturb the Menorin guidance complex. SAX-7/L1CAM, a hypodermal component of this complex, shows a male-specific expression pattern which precedes PVD extension, and its presence allows PVD to enter the tail rays. Further, our results reveal that genetically altered arborization or ablation of the PVD result in male mating behavioral defects, particularly as males turn around the hermaphrodite. These results uncover an adult-stage sexual dimorphism of dendritic branching and uncover a new function for PVD in male sexual behavior.

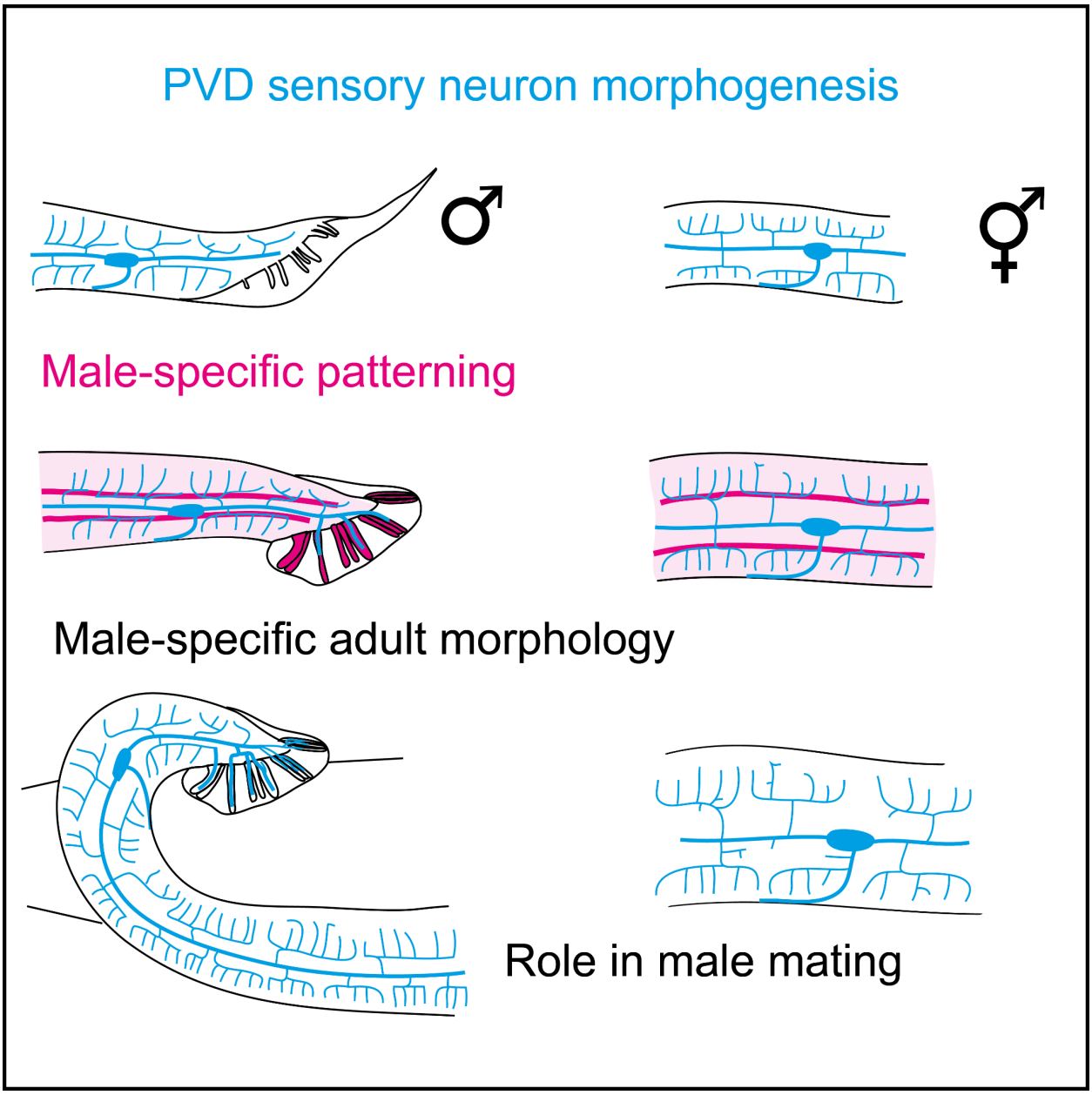

Graphical abstract

Keywords: PVD neuron; Sexual dimorphism; Male behavior; Dendrite arborization; *C. elegans;* SAX-7/L1CAM; Menorin complex

Introduction

Neurons grow distinctive morphologies and form sophisticated networks [1–5]. These networks often show sexual dimorphism, with different connectivity and distribution between the sexes [3,4,6–9]. In humans, multiple neurological disorders, including Parkinson's disease and dementia, are more prevalent in one sex [10]. While altered neuron shape, in particular dendritic spines, has been associated with some of these disorders [11–13], these differences are difficult to attribute to any sex-specific dendrite morphology .

The nematode *Caenorhabditis elegans* has been widely used as a model organism for studying neuron shaping [2,4,14], connectivity [2,3,15], plasticity [16–21] and activity [15,22,23]. While the majority of the wild type population are hermaphrodites, loss of one X chromosome yields males [24–26], which are sexually dimorphic in anatomy [27], neuronal connectivity [4], and behavior [24,28,29]. Both the hermaphrodite and the male's compact nervous system consists of diverse neuron types and morphologies, which enable a variety of behaviors [3] including oriented movement [30–32] and escape [15,33–36]. Uniquely, each neuron's identity and the connectome linking them together have been established [2–4]. A small population of neurons in *C. elegans* that presents highly arborized dendrites has served as a robust system for analyzing neuron patterning and development [37,38], among them the neuron pair PVD [39–42].

Each of two PVD neurons (left and right) assumes its structure during the final three out of four larval stages of a hermaphrodite's development (L2-L4) [39,40] (Figure 1A-C). PVD is a polymodal sensory neuron, responding to noxious touch [34,39,43], temperature drops [44], sound vibration[36] and body position [45,46]. Its characteristic branching, forming repetitive subunits which resemble candelabra ('menorahs' [39]), develops through actin-mediated growth [47–49]. The hermaphrodite PVD morphogenesis is guided by the Menorin multipartite complex, in which transmembrane receptors from the PVD, notably the leucine-rich repeat transmembrane domain (LRR-TM) protein DMA-1 [50], bind hypodermal (epidermal) and muscle-expressed guidance cues, notably SAX-7/L1CAM, MNR-1/Menorin and LECT-2/Chondromodulin II [47,51–54]. Its initial branching is governed in part by a LIM homeobox domain transcription factor, MEC-3 [40,55–58]. In addition to the Menorin patterning complex, multiple pathways maintain neuron tiling, self-avoidance, and excessive branching pruning events, among them UNC-6/Netrin [49,59], KPC-1/Furin [60–62] and the cell-cell fusogen EFF-1 [39,63]. With age and following dendritic injury, PVD loses its characteristic form and develops excessive 'ectopic' branches, which extend beyond the young-adult form [19,64,65] (Figure 1C).

Sexually dimorphic behavior in *C. elegans* can arise from altered expression of sensory channels [66,67], variation in synaptic connectivity and strength [68,69] and different gene expression networks [29,70], some of which may already be active prior to sexual maturation [71]. To date, differences in dendritic arborization between hermaphrodite and male *C. elegans* have been characterized in the motoneuron PDB [72], but, to our knowledge, never in a sensory neuron. Here, we focus on PVD, and ask whether its complex arbor has any sexually dimorphic features. We show PVD develops a post-larval, male-specific element of dendrite morphology, which extends into the specialized rays of the male tail, previously thought to contain only two neurons (RnA and RnB) [27]. This post-larval morphogenesis is consistent with a sexually dimorphic distribution of the hypodermal patterning cue SAX-7/L1CAM, acting within the sexually-shared Menorin patterning complex previously characterized in the hermaphrodite [48,50–53,61,62,73,74]. We further show that in addition to its sensory functions in hermaphrodites, PVD is required for precise male mating behavior, revealing an additional sex-specific role. Our results uncover sexual dimorphism in PVD morphogenesis and function, which also open directions for studying adult-onset directed dendritic branching.

Results

PVD morphology is sexually dimorphic

While much is known about hermaphrodite PVD dendritic tree morphogenesis (Figure 1A-C) [39,40], it remains unclear whether males share the same structure, patterning mechanism, and function. To determine the wildtype (WT) PVD structure of the male, we imaged animals either from stocks continuously maintained with males [75] or carrying a *him-5(e1490)* background mutation which increases the male percentage [28]. We found that male PVD develops candelabra-shaped dendritic units during the latter larval stages, L3 and L4, similar to the hermaphrodite [39,40] (Figure 1A-F). Four branching orders are maintained; the male primary branch is compressed medially compared with the hermaphrodite (Videos S1, S2). Branch density relative to body length is higher in males (Figure 1G), with altered distribution of ectopic branching (Figure 1H). Interestingly, we noted that in adulthood male PVD further extends into the sexually dimorphic tail rays (Figure 1F), confirmed by flow of photoconvertible Kaede protein from the cell body (Figure S1A-I). The male tail rays support a specialized fan (Figure 1I) required for mating [76,77], and each of the nine bilateral rays was previously shown to contain only two neurons, RnA and RnB [27,78], leading us to explore further. We found that PVD does not enter the rays as they first form in the fourth larval stage (L4); rather, PVD ray extension takes place around the final L4-to-adult molting (Figure 1E,F). To determine whether this branching phenomenon is intrinsic to the male identity of PVD itself, we utilized cell-specific feminization [79] by expressing a dominantly active intracellular domain of TRA-2 receptor from a PVD promoter. This analysis revealed that the male-specific branching into the male tail rays is not dependent on the sex of PVD itself (Figure S1J,K), leading us to look into possible sex-shared mechanisms involved in its morphogenesis.

Hermaphrodite-characterized PVD patterning mutants show similar male phenotypes

To characterize the wild-type placement of PVD within the male tail fan region, we imaged a ventral view of an adult tail (Figure 2A, top) and traced both left and right PVD neurons (Figure 2A, bottom). This revealed the two PVDs maintain lateral tiling as in the hermaphrodite [39,80], extending into their respective sides (Figure 2A).

To directly establish where PVD extends within the ray itself, we turned to previously unpublished electron microscopy cross sections of a young adult WT ray 6, and were able to locate a third neuronal process, distinct from ray neurons RnA and RnB, progressing between the structural cell and the hypodermis (Figure 2B,C). This provides the first direct evidence for the existence of three neurites within a wild-type male tail ray.

The hermaphrodite PVD morphogenesis is guided by the Menorin multipartite complex, in which transmembrane receptors from the PVD, notably the leucine-rich repeat transmembrane domain (LRR-TM) protein DMA-1 [50], bind hypodermal (epidermal) and muscle-expressed guidance cues, notably SAX-7/L1CAM and MNR-1/Menorin, alongside LECT-2/Chondromodulin II [47,51–54]. Its initial branching is governed in part by a LIM homeobox domain transcription factor, MEC-3 [58]. To determine whether this mechanism is sexually shared, we imaged *eff-1(ok1021)*, *mec-3(e1338), sax-7(dz156), mnr-1(dz175), dma-1(tm5159)* and *lect-2(ok2617)* mutant male animals and found that these backgrounds show similar PVD morphogenesis defects to hermaphrodites [40,51,52,58] (Figure 2D-I). We also confirmed PVD genetic ablation has a similar effect in males (Figure 2K) [45]. These results reveal that the roles of *mec-3* and *eff-1* in PVD branching are sex-shared, and that the Menorin guidance pathway participates in male PVD morphogenesis. We note that PVD also fails to extend into the tail rays in these backgrounds (Figure 2L).

Ray width is the determining factor for PVD elaboration within a ray

The age-dependent post-larval extension of PVD into the rays (Figure 2L) presents a unique model to explore dendritic sculpting. To determine the effect of ray anatomy on this phenomenon, we studied *mab-20(bx61ts)*, which presents an increased percentage of joined ('fused') rays [81], where two or more rays are displaced and join to share an epidermal sheath [78]. Our analysis of joined rays revealed they often contained a single PVD dendritic process, which may turn or branch further within the ray (Figure 2J, Figure S2B-E). Indeed, the WT ray 6 is naturally wider [81], and shows the same phenomenon (Figure S2A,E). PVD extension into the ray itself is not dependent on its width, as *mab-20(bx61ts)* remains comparable with WT (Figure 2L). This suggests ray placement has little effect on subsequent PVD extension, but wider rays allow a single PVD dendrite to elaborate further (Figure S2E).

PVD dendrite entry into tail rays is affected by tail morphology and the fusogen eff-1

To determine how overall tail morphology and PVD dendrite extension interact, we examined mutants of the epithelial fusogen *eff-1* which governs the correct formation of the syncytial hypodermis [82]. Mutants of *eff-1* show deformed tails, with a small fan and short rays [82] . In hermaphrodites, PVD is characteristically hyperbranched, extending multiple ectopic branches [39], a phenotype we note is also true for males (Figure 2D, Figure S2H). In males, however, this hyperbranching does not confer enhanced branching into the tail rays (Figure 2L). Rather, loss of *eff-1* inhibits this extension in a dosage-dependent manner, as established by comparison of *eff-1(hy21ts)* temperature-sensitive allele at restrictive and permissive temperatures (Figure S2F-I). While impaired, *eff-1* PVD ray extension rises with animal age (Figure S2J) as in the WT, indicating the neuron remains dynamic yet inhibited by the surrounding deformities.

Ray neurons RnBs are independent of PVD dendrites

To date, two neurons innervating the male tail rays were identified, named RnA and RnB (each numbered n=1-9 and bilateral; R1A(R/L), R2A(R/L) etc.) [27]. To study whether ray 'resident' neurons such as RnBs and PVD branches are interdependent during tail morphogenesis, we constructed a strain co-expressing distinct fluorescent reporter proteins for RnB (GFP) and PVD (mCherry). We found that in L4 animals, as the rays are projecting, RnB is already present within each ray, while PVD is absent (Figure 3A-C, n=54 rays, Video S3). In adults, PVD was partially associated with RnB within the lumbar and pre-anal ganglions as well as the rays, which contain RnB but may or may not contain PVD (Figure 3D; n=92 adult rays). This conforms with our EM analysis, which indicates that, within each ray, PVD projects outside the main channel which harbors RnB (Figure 2B,C). We conclude that male PVD and RnB follow different patterning mechanisms, and their extension is temporally and spatially separated.

sax-7 hypodermal patterning guides PVD dendrite entry into the male tail rays

Noting the arborization defects seen in Menorin complex mutant backgrounds also inhibit PVD extension into the tail rays (Figure 2L), we wondered whether its patterning components are present in the developing rays, notably the axonal guidance molecule SAX-7/L1CAM [51,52,83]. We imaged males carrying an integrated low-copy number fosmid-based reporter for *sax-7* translation [54,84] and found that during L4, a *sax-7p*::*sax-7::GFP* signal is visible within the nascent rays (Figure 3E-F). This patterning precedes PVD extension (Figures 1E). In the adult, PVD signal follows over the tail ray SAX-7::GFP pattern, which is prominent in all the rays (as

also shown by [85]), (Figure 3G-I, n=113 rays). In addition to the loss of PVD branching in the rays of *sax-7* mutant animals (Figure 2F), this branching was restored by hypodermal-specific expression of the short SAX-7 isoform (Figure 3J-L), previously used to rescue the hermaphrodite PVD morphogenesis defects of *sax-7* mutants [51,52]. Thus, in male adults, *sax-7* expression in the ray hypodermis appears to guide the entry of PVD branches into the tail. These results suggest a model whereby the sexually dimorphic aspect of PVD morphogenesis utilizes components of the established intercellular guidance complex in the hermaphrodite [51,52,83], however with a male-specific distribution and at a heterochronic post-larval stage.

PVD initiates dendritic branching into the rays prior to the onset of male mating behavior

Male mating in *C. elegans* is a complex multi-step process, performed by a male animal upon encountering a hermaphrodite [77]. Its execution relies on male-specific neurons and neural circuits [3] which guide chemosensory sexual attraction [66,86] and mechanosensation [77,87,88] as well as on sexually-dimorphic anatomy, in particular the male tail [27,77,88]. Once it has located a hermaphrodite, the male circles around it tail-first until the tail makes contact with the hermaphrodite's vulva [77]. The male then inserts its two copulatory spicules and ejaculates sperm into the hermaphrodite's uterus [77]. PVD is not open to the external environment or known to play any chemosensory role, leading us to focus on steps in male mating behavior which may involve mechanosensation [34,39,57] and proprioception [45,46]. We chose to analyze three behavioral steps: 1) Contact recognition, which is the initial reversal in response to tail contact with a hermaphrodite; 2) precise turning around the head or tail of the hermaphrodite during backwards movement to maintain scanning for the vulva; and 3) stopping at the vulva (Figure 4A) [77].

Having observed that WT PVD enters into the tail rays, we sought to find whether this correlates with proficient mating ability. We found PVD branching into the tail rays precedes this behavior: L4 males, where PVD has not yet entered into the tail rays (Figure 2L), also lack a functional fan structure [27]. This meant the earliest age we could analyze was young adults that have just molted, where PVD is already detected in some rays (Figure 2L). At this stage, many of the males displayed poor contact recognition (Figure S3A, YA, Video S4, 9/45 showing no response at all). 24h later, the same animals (kept in isolation) showed an improvement in mating turning and vulva recognition, comparable with same-aged virgin males (Figure S3B,C, Video S4). Age therefore correlates with increased PVD entry into the tail rays (Figure S3D) and simultaneously contributes to mating performance (Figure S3E), although precise turning does not require a

high percentage of rays to contain PVD (Figure S3F) nor directly correlates with a specific ray (Figure S3G). Following this observation, we used one-day adult males which show robust mating behavior in the WT, in order to compare backgrounds with altered PVD morphology.

PVD affects male mating behavior

mec-3(e1338), sax-7(dz156), mnr-1(dz175) and *dma-1(tm5159)* show normal external tail morphology (Figure 2E-H). This led us to wonder whether male behavior would be hindered in those circumstances. Indeed, all four genetic backgrounds impair male mating (Figure S4), particularly in turning (Figure S4E-H). Combined, these results pointed to a potential role for PVD in a male-specific behavior, affected at least in part by its dendritic morphology.

As PVD may not be the only neuron affected in these backgrounds [55,57,85,89], we turned to a strain where PVD is specifically genetically ablated [45] by expression of *deg-3(u662)* dominant-negative mutation which induces neuron degeneration (in neurons which express DEG-3 nicotinic acetylcholine receptor subunit [90]) (Figure 2K). In the hermaphrodite, PVD genetic ablation results in altered crawling motion [45]. We found that in males with PVD genetic ablation, mating behavior was impaired in all three steps of hermaphrodite recognition, turning and vulva stopping (Figure 4). Together with the prominent behavior impairment seen in the above four mutant backgrounds, these results suggest the PVD plays a novel role in adult male mating behavior, in particular during turning steps which require proprioception.

Discussion

To our knowledge, very few examples in *C. elegans* exist where sex-shared neurons assume different dendritic morphology. A male-specific ectopic sprouting of the motoneuron PDB is one such example [72], with the sensory neuron PVD, as shown here, being the other. Our analysis revealed that while hermaphrodite PVD largely maintains its late L4 morphology in early adulthood [51,52], male PVD undergoes further extension in the posterior region into the male-specific tail rays in early adulthood (Figure 1F, Figure 2L). This represents a morphogenesis mechanism distinct from that of a ‘resident’ ray neuron, RnB (Figure 3A-D). This plastic development extends from the hermaphrodite guidance complex adopting a sexually dimorphic distribution, through ray-specific SAX-7 expression (Figure 3E-I). Our observations of PVD forking within wide rays (Figure S2A-E), its dependence on hypodermal SAX-7 (Figure 3I-L) and our novel electron microscopy analysis (Figure 2B,C), suggest PVD projects in relation to the

ray hypodermis. Association of PVD and RnB at the pre-anal ganglion region (Figure 3D) conforms with connectome studies, which suggest that synapses form between PVD and RnB [4]. In addition to developing a male-specific dendritic morphology, it is possible that sexually-dimorphic connectivity also occurs during early adulthood, in parallel with an improvement in mating behavior (Figure S3A-C). While PVD-PVC connectivity was followed in the hermaphrodite [91], it is important to note that much of our knowledge of PVD synaptic partners relies on a male electron microscopy series reconstruction, for which comparable hermaphrodite reconstructions are as yet missing [2,4].
Alongside 'dedicated' ray neurons such as RnA [88], we show that PVD is important for male contact response, turning around the hermaphrodite and vulva recognition (Figure 4).

Importantly, *sax-7* mutant males were previously shown to have defects in contact response as well as vulva location efficiency [85]. Recently, *kpc-1* mutants were also shown to have male mating defects alongside impaired PVD arborization in the tail region [92]. Our results provide evidence for additional male-specific behavioral defects (Figure S4) in animals with impaired PVD morphology (Figure 2E-H). While we cannot rule out the possibility that PVD branching in certain ray combinations is important for turning behavior, as was demonstrated by global ablations of all or some ray neurons [77,88], this is difficult to ascertain in WT adults (Figure S3G). PVD branching into the tail rays precedes a striking change in male mate-seeking behavior and mating capacity from L4 to adulthood (Figure S3D-F). While PVD activity and morphology are not the sole contributor of male sexual behavior [77,88,93], PVD may be modulated as part of a male-specific, adult-specific, learning process. Complete and specific ablation of the PVD results in male behavior defects (Figure 4), which are consistent with PVD's role as a proprioceptor [45,46,94], and extend the role of PVD in males.
Our results uncover a previously uncharacterized role for PVD in male mating behavior, and reveal a sexually dimorphic instance of post-larval specific branching into the male tail rays, which seems integral to the early adult dendritic arbor. Further work is required to directly establish the mechanisms regulating PVD ray entry, and to elucidate the direct function of this dendritic morphology together with body candelabra in proprioception and male behavior.

Acknowledgements

We are grateful to Yehuda Salzberg, Hagar Setty and Meital Oren for strains (EB1564, EB1271, EB1653, DA509, MOS81), plasmid (pMO32) and valuable advice regarding mating

experiments, to Kang Shen for TV15911, TV15916, TV19321 and pXD22, and to Millet Treinin for MF288. We thank Scott Emmons and Hannes Bülow for their valuable comments regarding PVD connectivity. Son Le Tho for preliminary analyses of sexual dimorphism in PVD branching. Shay Stern, Dan Cassel and Meital Oren for critically reading the manuscript. Some strains were obtained from the *Caenorhabditis* Genetics Center (CGC) which is funded by the NIH Office of Research Infrastructure Programs (P40 OD01440). Research in our lab has received funding from the Israel Science Foundation (2462/18, 2327/19, 178/20 and 1575/21 to B.P.) and Dirección General de Asuntos del Personal Academico, Programa de Estancias de Investigación (PREI), UNAM, Mexico City (B.P.). Electron microscopy was supported by NIH OD R24 010943 (D.H.H.)

Author contributions

Conceptualization, Y.I. and B.P.; Methodology, Y.I. and D.H.H.; Investigation, Y.I. and D.H.H.; Writing - Original Draft, Y.I. and B.P.; Writing - Review and Editing, Y.I., D.H.H., M.K. and B.P.; Funding acquisition, B.P.; Resources, D.H.H. and M.K.; Supervision, B.P.

Declaration of interests

The authors declare no competing interests.

Supplemental information

Document S1:
Figures S1–S4
Movie legends
Supplemental References
Video S1. Hermaphrodite traced PVD neuron rotation, related to Figure 1C
Video S2. Male traced PVD neuron rotation, related to Figure 1F
Video S3. Male PVD and RnB traced in the L4, related to Figure 3C
Video S4. Mating of WT young adult to adult transition, related to Figure S3

Figure legends

Figure 1 WT male PVD development shows post-larval sexual dimorphism

(A-C) Hermaphrodite PVD development in L4 through to adult. PVD branch orders are marked yellow in panel C. Anterior is left, ventral down. *ser2prom3::GFP* PVD marker. Scale bar is 50 µm. Related to video S1.

(D-F) Male PVD development in L4 through to adult; white numbers and arrows note tail ray pairs; PVD branch orders are marked yellow. *ser2prom3::GFP* PVD marker. Asterisk notes PVD branching into the phasmids. Scale bar is 50 µm. Related to Figure S1 and Video S2.

(G) Analysis of PVD branches. *t* test, Holm-Šídák multiple comparison correction. Black bars show mean, error bars show ±SD. $p<0.05$ (*), $p<0.01$ (**), $p<0.001$ (***); $p<0.0001$ (****).

(H) Ectopic branches around the cell body region in 1-day adult animals, normalized per 100 µm of the primary branch for the different branching orders; n=16 (6 PVDL,10 PVDR) hermaphrodite and n=12 (7 PVDL, 5 PVDR) males. *t* test, Holm-Šídák multiple comparison correction. Black bars show mean, error bars show ±SD (except male ectopic tertiaries and ectopic quaternaries, showing +SD).

(I) Cartoon depiction of the male tail organ; lateral view contains a tracing of the neuron in panel F: projection of three-dimensional trace, branch orders annotated blue (1°), purple (2°), red (3°), cyan (4°) and yellow (5° and 6° order ectopics); scale bar is 50 µm; PVD branch orders are marked in black following panel F. Scale bar is 50 µm.

Figure 2 Mutants affecting hermaphrodite PVD shape show similar male phenotypes

(A) Top: ventral view of a two-day adult male, *ser2prom3::GFP* PVD marker. Scale bar is 50 µm. Bottom: cartoon tracing of respective PVDL (blue) and PVDR (green). Arrows denote PVD branching into the rays.

(B) Cartoon depiction of a longitudinal section across a male tail ray, noting hypodermis (hyp), structural cell (str), fan cuticle and ray neurons RnA (magenta), RnB (orange) and PVD (cyan). Scale bar is 50 µm. Based on ([27]).

(C) Transmission electron microscopy image of a thin cross section of a young adult WT ray 6, noting hypodermis (hyp), structural cell (str), fan cuticle and ray neurons RnA (magenta), RnB (orange) and PVD (cyan) as in panel B. Scale bar is 1 µm.

(D) Male one-day adult *eff-1(ok1021); him-5(e1490); ser2prom3::GFP* PVD, white arrows mark (empty) residual rays. yellow arrows point to examples of characteristic altered hyperbranched structure.

(E) Male one-day adult *mec-3(e1338); him-5(e1490); ser2prom3::GFP* PVD*,* orange arrowhead marks the posterior-most branch. A white arrow points to a process of the PDE, most visible here but also present in panel D and Figure 1D,E (also see Materials and Methods).

(F) Male one-day adult *sax-7(dz156); pF49H12.4::GFP,* yellow arrows point to examples of characteristic altered structure, orange arrowhead marks the posterior-most branch.

(G) Male one-day adult *mnr-1(dz175); pF49H12.4::GFP*, yellow arrows point to examples of characteristic altered structure, orange arrowhead marks the posterior-most branch.

(H) Male one-day adult *dma-1(tm5159); pF49H12.4::GFP,* yellow arrow points to characteristic altered structure, orange arrowhead marks the posterior-most branch.

(I) Male one-day adult *lect-2(ok2617); ser2prom3::GFP*, yellow arrow points to characteristic altered structure, orange arrowhead marks the posterior-most branch.

(J) *mab-20(bx61ts); him-5(e1490); ser2prom3::GFP* 1-2-day adult at a semi-restrictive 22°C temperature, yellow arrow marks a characteristic 'fusion' joining rays 3 and 4.

(K) PVD genetic ablation *ser2prom3::deg-1(u662); him-5(e1490); ser2prom3::Kaede* two-day adult showing signal remnant (arrow) next to the PVD soma, corresponding to PDE, with ventral truncated axon-like process. (*him-5(e1490)* background). Scale bar is 50 µm.

(L) Quantification of PVD entry into the tail rays in different mutant backgrounds and ages; all animals assayed express the integrated *ser2prom3*::*GFP* PVD marker and are *him-5(e1490*), with the exception of *deg-3(u662)* genetic ablation which utilizes a Kaede fluorescent marker, *lect-2(ok2617)* which has no *him-5* background, and *sax-7(dz156), mnr-1(dz175)* and *dma-1(tm5159)* which express an integrated *pF49H12.4::GFP* PVD marker and are without *him-5*; YA: young adult; A1d, A1.5d, A2d, A3d, A4d: 1, 1.5, 2, 3 and 4-day adult, respectively. Day 1 adult = L4 + 1 day. n =15, 28, 10, 21, 11, 13, 10,11, 5, 10, 15, 12,12,13, respectively. For *mab-20(bx61ts)*, one day from L4 at room temperature is comparable with to L4 + 28 h at 20°C and

as such marked 1.5 day adult. One-way ANOVA, Šídák multiple comparison correction. Black bars show mean, error bars show ±SD. $p<0.05$ (*), $p<0.01$ (**), $p<0.001$ (***); $p<0.0001$ (****). Related to Figure S2.

Figure 3 RnB neuron and *sax-7*::GFP signal appear in rays prior to PVD extension
(A) L4 stage GFP signal of RnB marker *pkd-2::GFP* and PVD marker *pF49H12.4::mCherry*. RnB signal was observed in 54/54 nascent tail rays (excluding ray 6; yellow arrow), with 0/54 showing PVD signal.

(B) Respective DIC image of A.

(C,D) Merged images of PVD marker *pF49H12.4::mCherry* (pseudocolored cyan) and RnB marker *pkd-2::GFP* (pseudocolored magenta; see also Video S4) over DIC (gray) during late L4 (lateral view) and adult (dorsal view), respectively. RnB signal was observed in 92/92 adult tail rays (excluding ray 6), with PVD signal in 67/92 (of which nine cases of partial entry). Red arrows point to tail rays; yellow arrows indicate ray pair six, white arrowheads point to the pre-anal ganglion region. Related to Video S3.

(E, G) Male tail with *sax-7* reporter during development. Signal observed in 43/43 nascent (L4) rays.

(I) Adult lateral view of merged *sax-7* reporter with PVD marker, 'inverted' pseudo-colors are used for clarity. 113/113 one-day adult rays observed with SAX-7 signal, of which 79/113 with PVD signal.

(F, H) Matching DIC images to E,G,I, respectively. Red arrows point to tail rays. Scale bar is 50 µm.

(J) One day adult *sax-7(dz156); him-5(e1490)* male, *pF49H12.4::GFP,* injected with *dpy-7p::sax-7(s)* short variant [51,52]. Orange arrowhead marks the posterior-most branch, non-transgenic (Non-Tg) control. Scale bar is 50 µm.

(K) One day adult *sax-7(dz156); him-5(e1490)* male, *pF49H12.4::GFP,* injected with *dpy-7p::sax-7(s)* short variant [51,52] with co-injection marker (pharyngeal muscle *myo-2p::GFP*). Scale bar is 50 µm.

(L) Blind analysis of PVD entry into the male tail rays in animals carrying extrachromosomal *dpy-7p::sax-7(s)* short variant [51,52] comparing transgenic (Tg) with non-transgenic (Non-Tg) animals based on co-injection marker expression (pharyngeal muscle *myo-2p::GFP*). Unpaired *t* test, $p<0.05$ (*), $p<0.01$ (**). A1d one-day adult animals are analyzed from one transgenic line (n=16,10, respectively); adults are F1 progeny of several injected hermaphrodites (n=7, 12, respectively).

Figure 4 Mating behavior is impaired under PVD genetic ablation

(A) Cartoon of mating steps. Male presented in purple, hermaphrodite in green.

(B-D) Hermaphrodite recognition, turning and vulva recognition, respectively, in WT and *ser2prom3*::*deg-3(u662)* animals where PVD undergoes early degeneration. B: n=18 WT, n=18 *ser2prom3*::*deg-3(u662)*; C: n=16 WT, 18 *ser2prom3*::*deg-3(u662)*; D: n=18 WT, 18 *ser2prom3*::*deg-3(u662)*. Perfect turn is defined as a turn completed successfully without the male tail losing contact with the hermaphrodite. *t* test, black bars show mean, error bars show ±SD. $p<0.05$ (*), $p<0.01$ (**), $p<0.0001$ (****).

Resource availability

Lead contact

Further information and requests for resources and reagents should be directed to and will be fulfilled by lead contact, Benjamin Podbilewicz (podbilew@technion.ac.il)

Materials availability

Strains created in this study are available upon request from the lead contact

Data and code availability

All the data used in this study is available from the lead contact upon request. This paper does not utilize any original code.

MATERIALS AND METHODS

EXPERIMENTAL MODEL AND STUDY PARTICIPANT DETAILS

A complete list of strains used in this study is found in the Key Resource Table.

Worms were kept at 20°C unless specified, on NGM plates with 150 µl OP50 *Escherichia coli* grown overnight in LB medium, using standard methods [95]. Males which are not from a *him-5(e1490)* genetic background were obtained by subjecting L4 hermaphrodites to 32°C for obtaining a higher incidence of spontaneous males [28], which were then propagated with non-heat-treated hermaphrodites. Synchronized experiments were set by picking 10-15 adult hermaphrodites onto a plate to lay eggs (room temperature, 22-23°C), and their removal after 1-2 h. Two days later, L4 animals were picked based on external appearance. Day 1 of adulthood is considered L4 + 1 day. For experiments involving males kept from heat shock plates with no underlying genetic *him-5* background [24], same-aged animals were selected from a mixed-age plate by picking L4-stage animals based on external appearance of the retracting-stage, swollen tail [96], or synchronized by placing hermaphrodites from male-rich plates with additional males on a plate and their removal after 3 h. Hermaphrodites used in mating were separated as L4 based on a "Christmas tree" vulva (~40 h from hatching, see figure 18 of [97]) or slightly older. *eff-1* strains, which are slower to grow, were aged based on L4 morphology, see '*eff-1* development' section. Young adult males just after molting were obtained by either synchronized 48 h growth at room temperature, observing the molted cuticles, or by 2.5 days at 20°C selecting and observing L4 animals in 1-2 h intervals until molted. Males were scored for mating behavior 1-6 h after molting, kept in isolation, and re-evaluated after 24h.

METHOD DETAILS

Transgenic lines

Transgenic animals were obtained by microinjection [98]. PVD feminization was analyzed in two separate transgenic lines. Hypodermal *dpy-7p::sax-7(s)* rescue experiments analyzed one transgenic line as one-day adults (L4+1 day) and in adult F1 progeny of multiple other injected hermaphrodites. Two additional transgenic lines were sampled as one- or two-day adults to confirm PVD extension into the rays (2/6 and 2/3 transgenic animals, respectively, with 6 and 1 non-transgenic controls showing no PVD extension into the tail region).

Electron microscopy

Electron microscopy was performed as described in [78]. The transverse section used in this work belongs to the same animal and same ray depicted in Fig. 2C of [78], which shows a more distal section, in which PVD is no longer visible. The PVD was followed over several sections and is distinct from the ray neurons RnA and RnB, tapering towards the end of the ray and generally thinner than RnA and RnB. It has a clear cytoplasm, elongated outline when viewed from the side, or closer to circular when viewed in cross-section, and few to no microtubules. From the sections observed, PVD tends to run inserted between the hypodermis and the structural cell.

Mating assays

Mating was scored following [77], and experiments set up as published previously [68]. When scoring turning behavior, a 'perfect' turn was defined as a turn completed successfully without the male tail losing contact with the hermaphrodite (see 'good turn' vs 'sloppy turn' in Figure 4

[99]). L4-stage males (wild type and test group) and *unc-31(e928)* hermaphrodites were picked a day prior to the experiment, kept separately. NGM plates were seeded with a single drop (~10 µl) OP50. The following day (approximately 16 h later), with the OP50 dried to a matte finish, 15 hermaphrodites were transferred onto a plate. Male plates (wild type and test group) were coded and then blinded by a second person, which had no knowledge of their genotype. For each experiment, a single male animal was placed just outside the OP50 spot using an eyelash attached to a toothpick on the plate and monitored under a dissecting scope for 15 minutes from the first tail contact of a hermaphrodite, or until mated (if sooner). Animals which did not approach within one body-length away from a hermaphrodite after five minutes were repositioned with an eyelash. Mated hermaphrodites were replaced. For some experiments, animals which displayed difficulty with spicule insertion, a step which may depend on the hermaphrodite used [77], were assayed on a second hermaphrodite for an additional 15 minutes or until mated, typically by removing the first hermaphrodite and allowing the male to locate a second mate on the plate. Cases where two hermaphrodites were used were pooled together to collect the overall male behavior in both attempts. Males were assayed alternating between both blinded test groups to avoid a batch effect due to different age or plate condition. Assays for young adult-to-adult transition utilized a single hermaphrodite per male. All experiments involved manual annotation of the mating sequence *in situ*. Most experiments were recorded using a Hamamatsu Orca-ER EMCCD camera using Micromanager 2.0 (ImageJ, NIH), set at 2x2 binning, imaging 1000 frames per 04:15 minute video; several such videos were captured for each mating. Spicule insertion and sperm transfer were definitively established for most of the experiments, by using a Zeiss SteREO Discovery.V8 dissecting scope. Mating efficiency (number of progeny sired [28]) was not determined.

Importantly and as noted in [100], animal mounting (see 'Imaging') utilized tetramisole (levamisole), which induces spicule protraction. This effect was at times irreversible and led to mating defects in cases where the animals were re-evaluated (data not shown). To mitigate this, these animals were closely observed prior to mating contact, and were censored if the spicules were protracted. The improved behavior of young animals, assayed twice (which did not show spicule extension) indicates that the mounting, imaging and recovery process by itself does not significantly harm male mating behavior.

Imaging

Worms were typically immobilized in 0.05% tetramisole (Sigma T1512) in M9 buffer [95]. Briefly, a 3% agar pad was prepared (Bacto-Agar in DDW) and worms were loaded onto a 4 µl drop of tetramisole placed directly on the pad. A coverslip was then secured with thin strips of marking tape. Tetramisole is the racemic mixture of the 20-fold more active form levamisole and dexamisole [101,102], making 0.05% tetramisole (2 mM) roughly comparable to 1 mM levamisole. In rare cases and for brief imaging sessions where animals were not recovered, animals were similarly mounted in 30 mM sodium azide (Sigma S2002) in DDW [BP2297 *ddIs290; him-5(e1490)*]. Male PVD morphology in L4 WT is not observably altered by the use of tetramisole compared with sodium azide mounting, although thin quaternary branches are somewhat clearer in azide mounting (data not shown).

Animals were imaged using one of two microscope systems: 1) an inverted confocal microscope (Nikon Ti Eclipse) with a CSU-X spinning disk unit (Yokogawa), and either a Plan-Fluor oil 40X NA 1.3 or oil 60x NA 1.4 (Nikon) objective, capturing serial z-axis sections spaced 0.6 µm apart captured by an iXon3 or iXon Ultra EMCCD camera (Andor, Belfast), using Metamorph (version 7.8.1.0, Molecular Devices); 2) an inverted confocal microscope (Nikon Eclipse Ti-2) with a CSU-W1 spinning disk unit (Yokogawa) equipped with a water Plan-Apochromat 60X NA 1.2 objective (CFI) capturing serial z-axis sections spaced 0.3 µm apart using a Prime BSI sCMOS camera (Teledyne Photometrics) through NIS-Elements AR interface software (Nikon). GFP and Kaede were imaged using 488 nm laser excitation, mCherry and photoconverted Kaede were imaged using 561 nm laser excitation. Kaede photoconversion was performed by 405 nm laser excitation. Experiments where both PVD neurons were imaged involved opening the slide, adding a drop of M9 buffer, repositioning the animal using an eyelash, and replacing the coverslip. Animals which were to be imaged again at a later time point were similarly removed from the slide and placed to recover on an NGM plate with OP50 as described.

Neuron tracing

Neuron tracing was performed on three-dimensional stacks semi-manually by the Fiji plugin SNT 3.2.3 (Plugins → Neuroanatomy → SNT) 103 and colored manually within the software. Rotation videos of such tracings were obtained using the software's 3D viewer. Cell placements (*e.g.* RnB cell bodies) were traced manually using the Fiji Cell Counter plugin on a three-dimensional image stack, subsequently projected to the XY plane. For figure clarity, this projection was then manually traced over in a thicker stroke.

The *ser2prom3::GFP* marker labels the sensory PDE neuron as well, whose cell body is adjacent to PVD [56]. PDE sends an anterior but also a posterior ventral process [2], observable in males, but also hermaphrodites, as elegantly shown by O'Brien et al., [56]. It appears most clearly here (as annotated by a white arrow) in Figure 2E, but can also be seen in Figure 2D and Figure 1D,E.

eff-1 development time calibration at different temperatures

Development timing assessment of WT animals was obtained from [104,105], yielding roughly consistent ratios between 16°C, 20°C and 25°C, with roughly 25% of pre-adult development spent as L4 (26±1.7%) [105]. Development time at 16°C can be corrected to an equivalent 20°C dividing by 1.6 and 25°C corrected to 20°C dividing by 0.76 [105]. We used 16°C values for growth at 15°C (correction factor 1.6), and the mean of 20°C and 25°C for growth at room temperature (22-23°C) (correction factor 0.87). *eff-1* animals grow somewhat slower than WT [39], and the null mutant *ok1021* at 20°C seemed to reach young adulthood after 72 h. Based on this time point and assuming the proportion of time spent at each developmental stage is WT-like, we obtained the following values for approximate development rate in hours:

Table 1: *eff-1* approximate development time in hours inferred from WT development ratios [105] and based on the null *eff-1(ok1021)* mutant reaching L4-young adult at 20°C after three days.

eff-1 hours from egg laid	15°C (Values by 16°C)	20°C	25°C	Room temperature 22-23°C
L4/Adult molt	114	72	55	63
Mid L4	99	63	48	55
L4 + 24 h (1 day adult)	123	87	72	78

These values were used to estimate hours of development in cases where animals were selected based on L4 appearance and analyzed the following day; the real hours of development were subsequently converted to the (hypothetical) 20°C equivalent by the correction ratios mentioned above.

PVD-specific genetic ablation and interacting neurons

While the RnB-specific *pkd-2::GFP* used does not mark R6B [106–108], a cross of the genetic ablation strain into a *pkd-2::GFP* strain reveals all other RnB neurons are unaffected. While we cannot directly establish whether R6B is affected by the *ser2prom3*::*deg-3(u662)* construct through gap junction interactions, no vacuolated neurons were observed by DIC in the lumbar ganglion. Additionally, while killing of electrically-coupled neurons to those expressing *deg-3(u662)* has been hinted [109], the PVD is strongly associated with the CAN neuron [2,4], which, although its precise function remains unclear, has a lethal rod-shape phenotype when ablated [2,110], which was not observed.

No data was found regarding *deg-3* expression in male ray neurons, however hermaphrodite RNA sequencing data is available at the single neuron level (https://cengen.shinyapps.io/CengenApp/ ; [111]). This data supports the hypothesis in [45], which the OLL neuron pair, the only other observable neuron expressing a *ser-2prom3* reporter [45,58], is not degenerated in *ser2prom3*::*deg-3(u662)* animals since it expresses ~100-fold less *deg-3* (https://cengen.shinyapps.io/CengenApp/; [111]). Based on hermaphrodite data, body muscles express similarly low levels of *deg-3* (https://cengen.shinyapps.io/CengenApp/; [111]). This tentatively supports the notion that muscles are likely unaffected by ectopic *deg-3(u662)* even if low expression of *ser2prom3* is present (a different *ser-2* promoter region, *ser2prom1*, is expressed in a sexually-dimorphic fashion in male posterior muscles, including the diagonal muscles used in mating [58]).

QUANTIFICATION AND STATISTICAL ANALYSIS

Image analysis and quantification

Analysis of male tail rays for neuron presence was manually evaluated using Fiji (ImageJ, NIH) by merging DIC and fluorescent channels and following the fluorescent signal through the Z-series in three dimensions. Rays which were not clearly visible by DIC were not scored. Most

animals were captured in a lateral view; the distal PVD neuron was typically difficult to analyze, hence some animals have data for one side but not the other. Experiments specifically designed to observe both left and right sides required opening the slide and gently manipulating the animals in a drop of M9 buffer using an eyelash attached to a toothpick. The figures presented are Z-axis projections, typically with DIC pseudo-colored magenta and fluorescent signal pseudo-colored cyan. Transgenic lines were imaged alongside non-transgenic siblings and analyzed blindly.

Images were edited for brightness, contrast, correct scaling and channel merging using Fiji (imageJ, NIH). Images of neurons are maximal-intensity projections across a Z-series stack, while DIC images are a single Z position. Figures were prepared using Adobe Illustrator CS5 (Adobe Inc.). Plots were prepared using GraphPad Prism (9.0.2).

Analysis of PVD orders was performed on image series taken around or just anterior to the cell body, by manual annotation using the Fiji Cell Counter plugin (Plugins → Analyze → Cell Counter → Cell Counter) on a three-dimensional image stack. Different counter types were renamed for each branching order, and final counts were manually copied.

Statistics

All statistical tests were performed using GraphPad Prism (9.0.2). Unless specified otherwise, p values are represented in asterisks as follows: $p<0.05$ (*), $p<0.01$ (**), $p<0.001$ (***); $p<0.0001$ (****). Specific tests are described individually for each figure.

KEY RESOURCES TABLE

REAGENT or RESOURCE	SOURCE	IDENTIFIER
Bacterial and virus strains		
***Escherichia coli* strain OP50**	**CGC https://cgc.umn.edu/strain/OP50 As described by Brenner** [24]	**OP50**
Chemicals, peptides, and recombinant proteins		

Tetramisole	**Sigma**	**T1512**
Sodium Azide	**Sigma**	**S2002**
Experimental models: Organisms/strains		
***C. elegans* N2**	**CGC** **https://cgc.umn.edu/strain/N2**	**N2**
hmnIs133[ser2prom3::Kaede]	**Kravtsov et al.,** [64]**,** **Yip and Heiman** [80]	**BP709**
hmnIs133[ser2prom3::Kaede]; him-5(e1490) V	**Inberg et al.,** [112]	**BP1021**
eff-1(hy21) II	**Oren-Suissa et al.,** [39]	**BP75**
eff-1(ok1021) II; mec-4(e1611) X	**Podbilewicz Lab**	**BP462**
him-5(e1490) V	**CGC** **https://cgc.umn.edu/strain/DR466**	**DR466**
mab-20(bx61ts) I; him-5(e1490) V.	**CGC** **https://cgc.umn.edu/strain/EM253** **Baird et al.,** [81]	**EM253**
wdIs52[pF49H12.4::GFP unc-119(+)]	**CGC** **https://cgc.umn.edu/strain/NC1687** **Smith et al.,** [40]	**NC1687**
dma-1(tm5159) I; wdIs52[pF49H12.4::GFP unc-119(+)] II;	**Y. Salzberg** **Salzberg et al.,** [51]	**EB1564**
sax-7(dz156) IV ; wdIs52[pF49H12.4::GFP unc-119(+)] II;	**Y. Salzberg** **Salzberg et al.,** [51]	**EB1653**
mnr-1(dz175) V; wdIs52[pF49H12.4::GFP unc-119(+)] II	**Y. Salzberg** **Salzberg et al.,** [51]	**EB1271**
dzIs53[pF49H12.4::mCherry] II	**Ramirez et al.,** [113]	**EB1982**
bxIs14[pkd-2::GFP pdx-1]; him-5(e1490) V	**M. Oren** **Lints et al.,** [107]**, Barr and Sternberg** [108]	**MOS81**
ser2prom3::deg-3(u662) (integrated)	**M. Treinin** **Albeg et al.,** [45]	**MF288**
wyIs592[ser2prom3::myr-GFP odr-1::RFP] III	**K. Shen** **Dong et al.,** [61]	**TV15911**
lect-2(ok2617) II; wyIs592[ser2prom3::myr-GFP odr-1::RFP] III	**K. Shen** **Zou et al.,** [53]	**TV19321**
ddIs290[sax-7::TY1::EGFP::3xFLAG(92C12) *unc-119(+)]*	**CGC**	**TH502**

	https://cgc.umn.edu/strain/TH502 **Tang et al.,** [84]	
mec-3(e1338) IV	**CGC** https://cgc.umn.edu/strain/CB1338	**CB1338**
unc-31(e928) IV	**M. Oren** **Oren-Suissa et al.,** [68] **CGC** https://cgc.umn.edu/strain/DA509	**DA509**
ser2prom3::deg-2(u662) (integrated); *him-5(e1490); hmnIs133[ser2prom3::Kaede]*	This work MF288 x BP1021♂	**BP2283**
him-5(e1490) V; wyIs592[ser2prom3::myr-GFP podr-1::RFP] III	This work TV15911 x (N2 x BP1021 ♂) ♂	**BP2285**
bxIs14[pkd-2::GFP + pdx-1]; him-5(e1490) V; dzIs53[pF49H12.4::mCherry] II	This work EB1982 x MOS81♂	**BP2287**
mec-3(e1338) IV; him-5 (e1490) V; wyIs592[ser2prom3::GFP podr-1::RFP]	This work BP2279 x BP2285 ♂	**BP2290**
*eff-1(ok1021) II; him-5 (e1490) V; wyIs592[ser2prom3::myr-GFP podr-1::*RFP*] III;*	This work BP462 x BP2285 ♂	**BP2291**
mab-20(bx61) I; *him-5(e1490) V*; *wyIs592[ser2prom3::myr-GFP podr-1::RFP] III*	This work EM253 x BP2285 ♂	**BP2293**
ser2prom3::deg-3(u662); *him-5(e1490) V; bxIs14[pkd-2::GFP pdx-1]; hmnIs133[ser2prom3::Kaede]*	This work BP2283 x MOS81 ♂	**BP2294**
eff-1(hy21) II; him-5(e1490); *wyIs592[ser2prom3::myr-GFP podr-1::RFP] III*	This work BP75 x BP2285 ♂	**BP2295**
eff-1(hy21) II; *bxIs14[pkd-2::GFP pdx-1]*; *him-5(e1490) V*;	This work BP2295 x MOS81 ♂	**BP2296**
ddIs290[sax-7::TY1::EGFP::3xFLAG(92C12) + unc-119(+)]; him-5(e1490) V	This work TH502 x DR466 ♂	**BP2297**
dzIs53[pF49H124::mCherry]/+ II; ddIs290[sax-7::TY1::EGFP::3xFLAG(92C12) + unc-119(+)] /+; him-5(e1490) V	This work EB1982 x BP2297 ♂	**BP2298**
wyIs592[ser2prom3::myr-GFP; podr-1::RFP] III; him-5(e1490) V; hyEx415[pYI8(ser2prom3::tra-2(ic)::SL2::2xNLS-TagRFP) 20 ng/ul pmyo-2::GFP 10 ng/ul pBluescript KS 70 ng/ul]	This work BP2285 microinjection	**BP2299**

wyIs592[ser2prom3::myr-GFP; podr-1::RFP] III; him-5(e1490) V; hyEx442[pYI8(ser2prom3::tra-2(ic)::SL2::2xNLS-TagRFP) 20 ng/ul pmyo-2::GFP 10 ng/ul pBluescript KS 70 ng/ul]	This work BP2285 microinjection	**BP2532**
wdIs52[pF49H12.4::GFP unc-119(+)] II; sax-7(dz156) IV ;him-5(e1490) V	This work EB1653 x DR466 ♂	**BP2355**
wdIs52[pF49H12.4::GFP unc-119(+)] II; sax-7(dz156) IV ;him-5(e1490) V; hyEx445: [dpy-7p::sax-7(s) 20 ng/ul myo-2p::GFP 10 ng/ul pBluescript KS 70 ng/ul] I	This work BP2355 microinjection	**BP2356**
Recombinant DNA		
ser2prom3::tra-2(ic)::SL2::2xNLS-TagRFP	**This paper** **pMO32 from Oren-Suissa et al.,** [68]	**pYI8**
dpy-7p::sax-7(s)	**Dong *et al.*,** [52]	**pXD22**
Software and algorithms		
Fiji (ImageJ 2.1.0/1.53c, Java 1.8.0_172)	**ImageJ, NIH**	**Fiji (RRID:SCR_002285)** **http://fiji.sc**
Illustrator CS5	**Adobe**	**Adobe Illustrator (RRID:SCR_010279)** **http://www.adobe.com/products/illustrator.html**
Prism 9.0.2	**GraphPad**	**GraphPad Prism (RRID:SCR_002798)** **http://www.graphpad.com/**

References

1. Ghysen, A., Dambly-Chaudière, C., Aceves, E., Jan, L.-Y., and Jan, Y.-N. (1986). Sensory neurons and peripheral pathways in Drosophila embryos. Rouxs. Arch. Dev. Biol. *195*, 281–289.

2. White, J.G., Southgate, E., Thomson, J.N., and Brenner, S. (1986). The structure of the nervous system of the nematode Caenorhabditis elegans. Philos. Trans. R. Soc. Lond. B Biol. Sci. *314*, 1–340.

3. Jarrell, T.A., Wang, Y., Bloniarz, A.E., Brittin, C.A., Xu, M., Thomson, J.N., Albertson, D.G., Hall, D.H., and Emmons, S.W. (2012). The connectome of a decision-making neural network. Science *337*, 437–444.

4. Cook, S.J., Jarrell, T.A., Brittin, C.A., Wang, Y., Bloniarz, A.E., Yakovlev, M.A., Nguyen, K.C.Q., Tang, L.T.H., Bayer, E.A., Duerr, J.S., et al. (2019). Whole-animal connectomes of both Caenorhabditis elegans sexes. Nature *571*, 63–71.

5. Merritt, D.J., and Whitington, P.M. (1995). Central projections of sensory neurons in the Drosophila embryo correlate with sensory modality, soma position, and proneural gene function. J. Neurosci. *15*, 1755–1767.

6. Kimura, K.-I., Ote, M., Tazawa, T., and Yamamoto, D. (2005). Fruitless specifies sexually dimorphic neural circuitry in the Drosophila brain. Nature *438*, 229–233.

7. Ciofi, P., Leroy, D., and Tramu, G. (2006). Sexual dimorphism in the organization of the rat hypothalamic infundibular area. Neuroscience *141*, 1731–1745.

8. Cachero, S., Ostrovsky, A. D., Yu, J. Y., Dickson, B. J., & Jefferis, G. S. (2010). Sexual dimorphism in the fly brain. Curr Biol *20*, 1589–1601.

9. Sacher, J., Neumann, J., Okon-Singer, H., Gotowiec, S., & Villringer, A. (2013). Sexual dimorphism in the human brain: evidence from neuroimaging. Magn Reson Imaging, *31*, 366–375. https://doi.org/10.1016/j.mri.2012.06.007

10. Palanza, P., and Parmigiani, S. (2017). How does sex matter? Behavior, stress and animal models of neurobehavioral disorders. Neurosci. Biobehav. Rev. *76*, 134–143.

11. Kulkarni, V.A., and Firestein, B.L. (2012). The dendritic tree and brain disorders. Mol. Cell. Neurosci. *50*, 10–20.

12. Kasai, H., Ziv, N.E., Okazaki, H., Yagishita, S., and Toyoizumi, T. (2021). Spine dynamics in the brain, mental disorders and artificial neural networks. Nat. Rev. Neurosci. *22*, 407–422.

13. Forrest, M.P., Parnell, E., and Penzes, P. (2018). Dendritic structural plasticity and neuropsychiatric disease. Nat. Rev. Neurosci. *19*, 215–234.

14. Chalfie, M., and Thomson, J.N. (1979). Organization of neuronal microtubules in the nematode Caenorhabditis elegans. J. Cell Biol. *82,* 278-289.

15. Chalfie, M., Sulston, J.E., White, J.G., Southgate, E., Thomson, J.N., and Brenner, S.

(1985). The neural circuit for touch sensitivity in Caenorhabditis elegans. J. Neurosci. *5*, 956–964.

16. Cohn, J.A., Cebul, E.R., Valperga, G., Brose, L., de Bono, M., Heiman, M.G., and Pierce, J.T. (2020). Long-term activity drives dendritic branch elaboration of a C. elegans sensory neuron. Dev. Biol. *461*, 66–74.

17. Giordano-Santini, R., Kaulich, E., Galbraith, K.M., Ritchie, F.K., Wang, W., Li, Z., and Hilliard, M.A. (2020). Fusogen-mediated neuron−neuron fusion disrupts neural circuit connectivity and alters animal behavior. Proc. Natl. Acad. Sci. U. S. A. *117*, 23054–23065.

18. Giordano-Santini, R., Linton, C., and Hilliard, M.A. (2016). Cell-cell fusion in the nervous system: Alternative mechanisms of development, injury, and repair. Semin. Cell Dev. Biol. *60*, 146–154.

19. Oren-Suissa, M., Gattegno, T., Kravtsov, V., and Podbilewicz, B. (2017). Extrinsic repair of injured dendrites as a paradigm for regeneration by fusion in Caenorhabditis elegans. Genetics *206*, 215–230.

20. Schroeder, N.E., Androwski, R.J., Rashid, A., Lee, H., Lee, J., and Barr, M.M. (2013). Dauer-specific dendrite arborization in C. elegans is regulated by KPC-1/furin. Curr. Biol. *23*, 1527–1535.

21. Wicks, S.R., and Rankin, C.H. (1996). The integration of antagonistic reflexes revealed by laser ablation of identified neurons determines habituation kinetics of the Caenorhabditis elegans tap withdrawal response. Journal of Comparative Physiology - A Sensory, Neural, and Behavioral Physiology. *179,* 675-685.

22. Bargmann C. I. (2006). Chemosensation in C. elegans. *WormBook : the online review of C. elegans biology*, 1–29.

23. Yemini, E., Lin, A., Nejatbakhsh, A., Varol, E., Sun, R., Mena, G.E., Samuel, A.D.T., Paninski, L., Venkatachalam, V., and Hobert, O. (2021). NeuroPAL: A Multicolor Atlas for Whole-Brain Neuronal Identification in C. elegans. Cell *184*, 272–288.e11.

24. Brenner, S. (1974). The genetics of Caenorhabditis elegans. Genetics *77*, 71–94.

25. Hodgkin, J.A., and Brenner, S. (1977). Mutations causing transformation of sexual phenotype in the nematode Caenorhabditis elegans. Genetics *86*, 275–287.

26. Nigon, V., and Dougherty, E.C. (1949). Reproductive patterns and attempts at reciprocal crossing of Rhabditis elegans Maupas, 1900, and Rhabditis briggsae Dougherty and Nigon, 1949 (Nematoda: Rhabditidae). J. Exp. Zool. *112*, 485–503.

27. Sulston, J.E., Albertson, D.G., and Thomson, J.N. (1980). The Caenorhabditis elegans Male: Postembryonic Development of Nongonadal Structures. Dev. Biol. *78*, 542–576.

28. Hodgkin, J. (1983). Male Phenotypes and Mating Efficiency in Caenorhabditis Elegans. Genetics *103*, 43–64.

29. Salzberg, Y., Gat, A., and Oren-Suissa, M. (2021). One template, two outcomes: How does the sex-shared nervous system generate sex-specific behaviors? Curr. Top. Dev. Biol. *144*, 245–268.

30. Mori, I. (1999). Genetics of Chemotaxis and Thermotaxis in the Nematode Caenorhabditis elegans. Annu. Rev. Genet., 399–422.

31. Chatzigeorgiou, M., Bang, S., Hwang, S.W., and Schafer, W.R. (2013). Tmc-1 encodes a sodium-sensitive channel required for salt chemosensation in C. elegans. Nature *494*, 95–99.

32. Bretscher, A.J., Kodama-Namba, E., Busch, K.E., Murphy, R.J., Soltesz, Z., Laurent, P., and de Bono, M. (2011). Temperature, oxygen, and salt-sensing neurons in C. elegans are carbon dioxide sensors that control avoidance behavior. Neuron *69*, 1099–1113.

33. Hilliard, M.A., Bargmann, C.I., and Bazzicalupo, P. (2002). C. elegans responds to chemical repellents by integrating sensory inputs from the head and the tail. Curr. Biol. *12*, 730–734.

34. Li, W., Kang, L., Piggott, B.J., Feng, Z., and Xu, X.Z.S. (2011). The neural circuits and sensory channels mediating harsh touch sensation in Caenorhabditis elegans. Nat. Commun. *2*, 315.

35. Edwards, S.L., Charlie, N.K., Milfort, M.C., Brown, B.S., Gravlin, C.N., Knecht, J.E., and Miller, K.G. (2008). A novel molecular solution for ultraviolet light detection in Caenorhabditis elegans. PLoS Biol. https://doi.org/10.1371/journal.pbio.0060198.

36. Iliff, A.J., Wang, C., Ronan, E.A., Hake, A.E., Guo, Y., Li, X., Zhang, X., Zheng, M., Liu, J., Grosh, K., et al. (2021). The nematode C. elegans senses airborne sound. Neuron *109*, 3633–3646.e7.

37. Androwski, R.J., Asad, N., Wood, J.G., Hofer, A., Locke, S., Smith, C.M., Rose, B., and Schroeder, N.E. (2020). Mutually exclusive dendritic arbors in C. elegans neurons share a common architecture and convergent molecular cues. PLoS Genet. *16*, 1–23.

38. Inberg, S., Meledin, A., Kravtsov, V., Iosilevskii, Y., Oren-Suissa, M., and Podbilewicz, B. (2019). Lessons from Worm Dendritic Patterning. Annu. Rev. Neurosci. *42*, 365–383.

39. Oren-Suissa, M., Hall, D.H., Treinin, M., Shemer, G., and Podbilewicz, B. (2010). The fusogen EFF-1 controls sculpting of mechanosensory dendrites. Science *328*, 1285–1288.

40. Smith, C.J., Watson, J.D., Spencer, W.C., O'Brien, T., Cha, B., Albeg, A., Treinin, M., and Miller, D.M. (2010). Time-lapse imaging and cell-specific expression profiling reveal dynamic branching and molecular determinants of a multi-dendritic nociceptor in C. elegans. Dev. Biol. *345*, 18–33.

41. Halevi, S., McKay, J., and Palfreyman, M. (2002). The C.elegans ric-3 gene is required for maturation of nicotinic acetylcholine receptors. EMBO J. *21,* 1012-1020

42. Yassin, L., Samson, A.O., Halevi, S., Eshel, M., and Treinin, M. (2002). Mutations in the extracellular domain and in the membrane-spanning domains interfere with nicotinic acetylcholine receptor maturation. Biochemistry *41*, 12329–12335.

43. Cho, Y., Oakland, D.N., Lee, S.A., Schafer, W.R., and Lu, H. (2018). On-chip functional neuroimaging with mechanical stimulation in Caenorhabditis elegans larvae for studying development and neural circuits. Lab Chip *18*, 601–609.

44. Chatzigeorgiou, M., Yoo, S., Watson, J.D., Lee, W.H., Spencer, W.C., Kindt, K.S., Hwang, S.W., Miller, D.M., Treinin, M., Driscoll, M., et al. (2010). Specific roles for DEG/ENaC and TRP channels in touch and thermosensation in C. elegans nociceptors. Nat. Neurosci. *13*, 861–869.

45. Albeg, A., Smith, C.J., Chatzigeorgiou, M., Feitelson, D.G., Hall, D.H., Schafer, W.R., Miller, D.M., and Treinin, M. (2011). Molecular and Cellular Neuroscience C . elegans multi-dendritic sensory neurons : Morphology and function. Mol. Cell. Neurosci. *46*, 308–317.

46. Tao, L., Porto, D., Li, Z., Fechner, S., Lee, S.A., Goodman, M.B., Xu, X.Z.S., Lu, H., and Shen, K. (2019). Parallel Processing of Two Mechanosensory Modalities by a Single Neuron in C. elegans. Dev. Cell *51*, 1–15.

47. Chen, C.-H., Hsu, H.-W., Chang, Y.-H., and Pan, C.-L. (2019). Adhesive L1CAM-Robo Signaling Aligns Growth Cone F-Actin Dynamics to Promote Axon-Dendrite Fasciculation in C. elegans. Dev. Cell *49*, 490–491.

48. Zou, W., Dong, X., Broederdorf, T.R., Yasuda, R., Chen, B., Zou, W., Dong, X., Broederdorf, T.R., Shen, A., Kramer, D.A., et al. (2018). A dendritic guidance receptor complex brings together distinct actin regulators to drive efficient F-actin assembly and branching. Dev. Cell *45*, 362–375.e3.

49. Sundararajan, L., Smith, C.J., Watson, J.D., Millis, B.A., Tyska, M.J., and Miller, D.M., 3rd (2019). Actin assembly and non-muscle myosin activity drive dendrite retraction in an UNC-6/Netrin dependent self-avoidance response. PLoS Genet. *15*, e1008228.

50. Liu, O.W., and Shen, K. (2011). The transmembrane LRR protein DMA-1 promotes dendrite branching and growth in C. elegans. Nat. Neurosci. *15*, 57–63.

51. Salzberg, Y., Díaz-Balzac, C.A., Ramirez-Suarez, N.J., Attreed, M., Tecle, E., Desbois, M., Kaprielian, Z., and Bülow, H.E. (2013). Skin-derived cues control arborization of sensory dendrites in Caenorhabditis elegans. Cell *155*, 308–320.

52. Dong, X., Liu, O.W., Howell, A.S., and Shen, K. (2013). An Extracellular Adhesion Molecule Complex Patterns Dendritic Branching and Morphogenesis. Cell *155*, 296–307.

53. Zou, W., Shen, A., Dong, X., Tugizova, M., Xiang, Y.K., and Shen, K. (2016). A multi-protein receptor-ligand complex underlies combinatorial dendrite guidance choices in C. elegans. Elife *5*, 1–25.

54. Díaz-Balzac, C.A., Rahman, M., Lázaro-Peña, M.I., Martin Hernandez, L.A., Salzberg, Y., Aguirre-Chen, C., Kaprielian, Z., and Bülow, H.E. (2016). Muscle- and Skin-Derived Cues Jointly Orchestrate Patterning of Somatosensory Dendrites. Curr. Biol. *26*, 2397.

55. Chalfie, M., and Sulston, J. (1981). Developmental genetics of the mechanosensory neurons of Caenorhabditis elegans. Dev. Biol. *82*, 358–370.

56. O'Brien, B.M.J., Palumbos, S.D., Novakovic, M., Shang, X., Sundararajan, L., and Miller, D.M. (2017). Separate transcriptionally regulated pathways specify distinct classes of sister dendrites in a nociceptive neuron. Dev. Biol. *432*, 248–257.

57. Way, J.C., and Chalfie, M. (1989). The mec-3 gene of Caenorhabditis elegans requires its

own product for maintained expression and is expressed in three neuronal cell types. Genes and Development *3*, 1823–1833.

58. Tsalik, E.L., Niacaris, T., Wenick, A.S., Pau, K., Avery, L., and Hobert, O. (2003). LIM homeobox gene-dependent expression of biogenic amine receptors in restricted regions of the C. elegans nervous system. Dev. Biol. *263,* 81-102.

59. Smith, C.J., Watson, J.D., VanHoven, M.K., Colón-Ramos, D.A., and Miller, D.M. (2012). Netrin (UNC-6) mediates dendritic self-avoidance. Nat. Neurosci. *15*, 731–737.

60. Salzberg, Y., Ramirez-Suarez, N.J., and Bülow, H.E. (2014). The proprotein convertase KPC-1/furin controls branching and self-avoidance of sensory dendrites in Caenorhabditis elegans. PLoS Genet. *10*, e1004657.

61. Dong, X., Chiu, H., Park, Y.J., Zou, W., Zou, Y., Özkan, E., Chang, C., and Shen, K. (2016). Precise regulation of the guidance receptor DMA-1 by KPC-1/Furin instructs dendritic branching decisions. Elife *5*, 1–22.

62. Ramirez-Suarez, N.J., Belalcazar, H.M., Rahman, M., Trivedi, M., Tang, L.T.H., and Bülow, H.E. (2023). Convertase-dependent regulation of membrane-tethered and secreted ligands tunes dendrite adhesion. Development *150*, dev201208.

63. Zhu, T., Liang, X., Wang, X.-M., and Shen, K. (2017). Dynein and EFF-1 control dendrite morphology by regulating the localization pattern of SAX-7 in epidermal cells. J. Cell Sci. *130,* 4063-4071.

64. Kravtsov, V., Oren-Suissa, M., and Podbilewicz, B. (2017). The fusogen AFF-1 can rejuvenate the regenerative potential of adult dendritic trees by self-fusion. Development *144*, 2364–2374.

65. Brar, H.K., Dey, S., Bhardwaj, S., Pande, D., Singh, P., Dey, S., and Ghosh-Roy, A. (2022). Dendrite regeneration in C. elegans is controlled by the RAC GTPase CED-10 and the RhoGEF TIAM-1. PLoS Genet. *18*, e1010127.

66. Ryan, D.A., Miller, R.M., Lee, K., Neal, S.J., Fagan, K.A., Sengupta, P., and Portman, D.S. (2014). Sex, age, and hunger regulate behavioral prioritization through dynamic modulation of chemoreceptor expression. Curr. Biol. *24*, 2509–2517.

67. Setty, H., Salzberg, Y., Karimi, S., Berent-Barzel, E., Krieg, M., and Oren-Suissa, M. (2022). Sexually dimorphic architecture and function of a mechanosensory circuit in C. elegans. Nat. Commun. *13*, 1–15.

68. Oren-Suissa, M., Bayer, E.A., and Hobert, O. (2016). Sex-specific pruning of neuronal synapses in Caenorhabditis elegans. Nature *533*, 206–211.

69. Pechuk, V., Goldman, G., Salzberg, Y., Chaubey, A.H., Bola, R.A., Hoffman, J.R., Endreson, M.L., Miller, R.M., Reger, N.J., Portman, D.S., et al. (2022). Reprogramming the topology of the nociceptive circuit in C. elegans reshapes sexual behavior. Curr. Biol. *32*, 4372–4385.e7.

70. Barr, M.M., García, L.R., and Portman, D.S. (2018). Sexual Dimorphism and Sex Differences in Caenorhabditis elegans Neuronal Development and Behavior. Genetics *208*,

909–935.

71. Haque, R., Kurien, S. P., Setty, H., Salzberg, Y., Stelzer, G., Litvak, E., Gingold, H., Rechavi, O., & Oren-Suissa, M. (2024). Sex-specific developmental gene expression atlas unveils dimorphic gene networks in C. elegans. Nat Commun *15*, 4273.

72. Pereira, L., Aeschimann, F., Wang, C., Lawson, H., Serrano-Saiz, E., Portman, D.S., Großhans, H., and Hobert, O. (2019). Timing mechanism of sexually dimorphic nervous system differentiation. Elife *8*, e42078.

73. Rahman, M., Ramirez-Suarez, N.J., Diaz-Balzac, C.A., and Bülow, H.E. (2022). Specific N -glycans regulate an extracellular adhesion complex during somatosensory dendrite patterning. EMBO Rep. *23*, 1–17.

74. Liang, X., Dong, X., Moerman, D.G., Shen, K., and Wang, X. (2015). Sarcomeres Pattern Proprioceptive Sensory Dendritic Endings through UNC-52/Perlecan in C. elegans. Dev. Cell *33*, 388–400.

75. Singson, A., Hill, K.L., and L'Hernault, S.W. (1999). Sperm competition in the absence of fertilization in Caenorhabditis elegans. Genetics *152*, 201–208.

76. Barr, M.M., and Garcia, L.R. (2006). Male mating behavior. WormBook, 1–11.

77. Liu, K.S., and Sternberg, P.W. (1995). Sensory regulation of male mating behavior in Caenorhabditis elegans. Neuron *14*, 79–89.

78. Chow, K.L., Hall, D.H., and Emmons, S.W. (1995). The mab-21 gene of Caenorhabditis elegans encodes a novel protein required for choice of alternate cell fates. Development *121*, 3615–3626.

79. Mowrey, W.R., Bennett, J.R., and Portman, D.S. (2014). Distributed effects of biological sex define sex-typical motor behavior in Caenorhabditis elegans. J. Neurosci. *34*, 1579–1591.

80. Yip, Z.C., and Heiman, M.G. (2016). Duplication of a Single Neuron in C . elegans Reveals a Pathway for Dendrite Tiling by Mutual Repulsion. Cell Rep. *15*, 2109–2117.

81. Baird, S.E., Fitch, D.H.A., Kassem, I.A.A., and Emmons, S.W. (1991). Pattern formation in the nematode epidermis: Determination of the arrangement of peripheral sense organs in the C. elegans male tail. Development *113*, 515–526.

82. Mohler, W.A., Shemer, G., Del Campo, J.J., Valansi, C., Opoku-Serebuoh, E., Scranton, V., Assaf, N., White, J.G., and Podbilewicz, B. (2002). The type 1 membrane protein EFF-1 is essential for developmental cell fusion. Dev. Cell *2*, 355–362.

83. Heiman, M.G., and Bülow, H.E. (2024). Dendrite morphogenesis in Caenorhabditis elegans. Genetics. https://doi.org/10.1093/genetics/iyae056.

84. Tang, L.T.H, Trivedi, M., Freund, J., Salazar, C.J., Rahman, M., Ramirez-Suarez, N.J., Lee, G., Wang, Y., Grant, B.D., Bülow, H.E. (2021) The CATP-8/P5A-type ATPase functions in multiple pathways during neuronal patterning. PLoS Genet. 17(7):e1009475. doi: 10.1371/journal.pgen.1009475.

85. Kim, B., and Emmons, S.W. (2017). Multiple conserved cell adhesion protein interactions

mediate neural wiring of a sensory circuit in C. elegans. Elife *6*. https://doi.org/10.7554/eLife.29257.

86. Sakai, N., Iwata, R., Yokoi, S., Butcher, R.A., Clardy, J., and Tomioka, M. (2013). A Sexually Conditioned Switch of Chemosensory Behavior in C . elegans. PloS one *8*, e68676.

87. Zhang, H., Yue, X., Cheng, H., Zhang, X., Cai, Y., Zou, W., Huang, G., Cheng, L., Ye, F., and Kang, L. (2018). OSM-9 and an amiloride-sensitive channel, but not PKD-2, are involved in mechanosensation in C. elegans male ray neurons. Sci. Rep. *8*, 1–8.

88. Koo, P.K., Bian, X., Sherlekar, A.L., Bunkers, M.R., and Lints, R. (2011). The robustness of Caenorhabditis elegans male mating behavior depends on the distributed properties of ray sensory neurons and their output through core and male-specific targets. Journal of Neuroscience *31*, 7497–7510.

89. Wang, X., Kweon, J., Larson, S., and Chen, L. (2005). A role for the C. elegans L1CAM homologue lad-1/sax-7 in maintaining tissue attachment. Dev. Biol. *284*, 273–291.

90. Treinin, M., and Chalfie, M. (1995). A mutated acetylcholine receptor subunit causes neuronal degeneration in C. elegans. Neuron. *14,* 871-877.

91. Husson, S.J., Costa, W.S., Wabnig, S., Stirman, J.N., Watson, J.D., Spencer, W.C., Akerboom, J., Looger, L.L., Treinin, M., Miller, D.M., et al. (2012). Optogenetic Analysis of a Nociceptor Neuron and Network Reveals Ion Channels Acting Downstream of Primary Sensors. Curr. Biol. *22*, 743–752.

92. Shih, M., Zou, Y., Ferreira, T., Suzuki, N., Kim, E., Chuang, C.-F., and Chang, C. (2024). The kpc-1 3′UTR facilitates dendritic transport and translation efficiency of mRNAs for dendrite arborization of a mechanosensory neuron important for male courtship. PLoS Genet. *20*, e1011362.

93. Susoy, V., Hung, W., Witvliet, D., Whitener, J.E., Wu, M., Park, C.F., Graham, B.J., Zhen, M., Venkatachalam, V., and Samuel, A.D.T. (2021). Natural sensory context drives diverse brain-wide activity during C. elegans mating. Cell *184*, 5122–5137.e17.

94. Cohen, E., Yemini, E., Schafer, W., Feitelson, D.G., and Treinin, M. (2012). Locomotion analysis identifies roles of mechanosensory neurons in governing locomotion dynamics of C. elegans. J. Exp. Biol. *215*, 3639–3648.

95. Stiernagle, T. (2006). Maintenance of C. elegans. WormBook. https://doi.org/10.1895/wormbook.1.101.1.

96. Nguyen, C.Q., Hall, D.H., Yang, Y., and Fitch, D.H.A. (1999). Morphogenesis of the Caenorhabditis elegans male tail tip. Dev. Biol. *207*, 86–106.

97. Sulston, J.E., and Horvitz, H.R. (1977). Post-embryonic cell lineages of the nematode, Caenorhabditis elegans. Dev. Biol. *56*, 110–156.

98. Evans, T. (2006). Transformation and microinjection. WormBook, 1–15.

99. Loer, C.M., and Kenyon, C.J. (1993). Serotonin-deficient mutants and male mating behavior in the nematode Caenorhabditis elegans. J. Neurosci. *13*, 5407–5417.

100. Garcia, L.R., Mehta, P., and Sternberg, P.W. (2001). Regulation of distinct muscle behaviors controls the C. elegans male's copulatory spicules during mating. Cell *107*, 777–788.

101. Lewis, J.A., Wu, C.H., Berg, H., and Levine, J.H. (1980). The genetics of levamisole resistance in the nematode Caenorhabditis elegans. Genetics *95*, 905–928.

102. Lewis, J.A., Wu, C.H., Levine, J.H., and Berg, H. (1980). Levamisole-resistant mutants of the nematode Caenorhabditis elegans appear to lack pharmacological acetylcholine receptors. Neuroscience *5*, 967–989.

103. Arshadi, C., Günther, U., Eddison, M., Harrington, K.I.S., and Ferreira, T.A. (2021). SNT: a unifying toolbox for quantification of neuronal anatomy. Nat. Methods *18*, 374–377.

104. Byerly, L., Cassada, R.C., and Russell, R.L. (1976). The life cycle of the nematode Caenorhabditis elegans. Dev. Biol. *51*, 23–33.

105. Lewis, J.A., and Fleming, J.T. (1995). Chapter 1: Basic Culture Methods. Methods Cell Biol. *48*, 3–29.

106. Jia, L., and Emmons, S.W. (2006). Genes that control ray sensory neuron axon development in the Caenorhabditis elegans male. Genetics *173*, 1241–1258.

107. Lints, R., Jia, L., Kim, K., Li, C., and Emmons, S.W. (2004). Axial patterning of C. elegans male sensilla identities by selector genes. Dev. Biol. *269*, 137–151.

108. Barr, M.M., and Sternberg, P.W. (1999). A polycystic kidney-disease gene homologue required for male mating behaviour in C. elegans. Nature *401*, 386–389.

109. Van Buskirk, C., and Sternberg, P.W. (2007). Epidermal growth factor signaling induces behavioral quiescence in Caenorhabditis elegans. Nat. Neurosci. *10*, 1300–1307.

110. Sundaram, M.V., and Buechner, M. (2016). The Caenorhabditis elegans excretory system: A model for tubulogenesis, cell fate specification, and plasticity. Genetics *203*, 35–63.

111. Taylor, S.R., Santpere, G., Weinreb, A., Barrett, A., Reilly, M.B., Xu, C., Varol, E., Oikonomou, P., Glenwinkel, L., McWhirter, R., et al. (2021). Molecular topography of an entire nervous system. Cell *184*, 4329–4347.e23.

112. Inberg, S., Iosilevskii, Y., and Podbilewicz, B. (2018). Sensory experience controls dendritic structure and behavior by distinct pathways involving degenerins. bioRxiv. https://doi.org/10.1101/436758.

113. Ramirez-Suarez, N.J., Belalcazar, H.M., Salazar, C.J., Beyaz, B., Raja, B., Nguyen, K.C.Q., Celestrin, K., Fredens, J., Færgeman, N.J., Hall, D.H., et al. (2019). Axon-Dependent Patterning and Maintenance of Somatosensory Dendritic Arbors. Dev. Cell *48*, 229–244.e4.

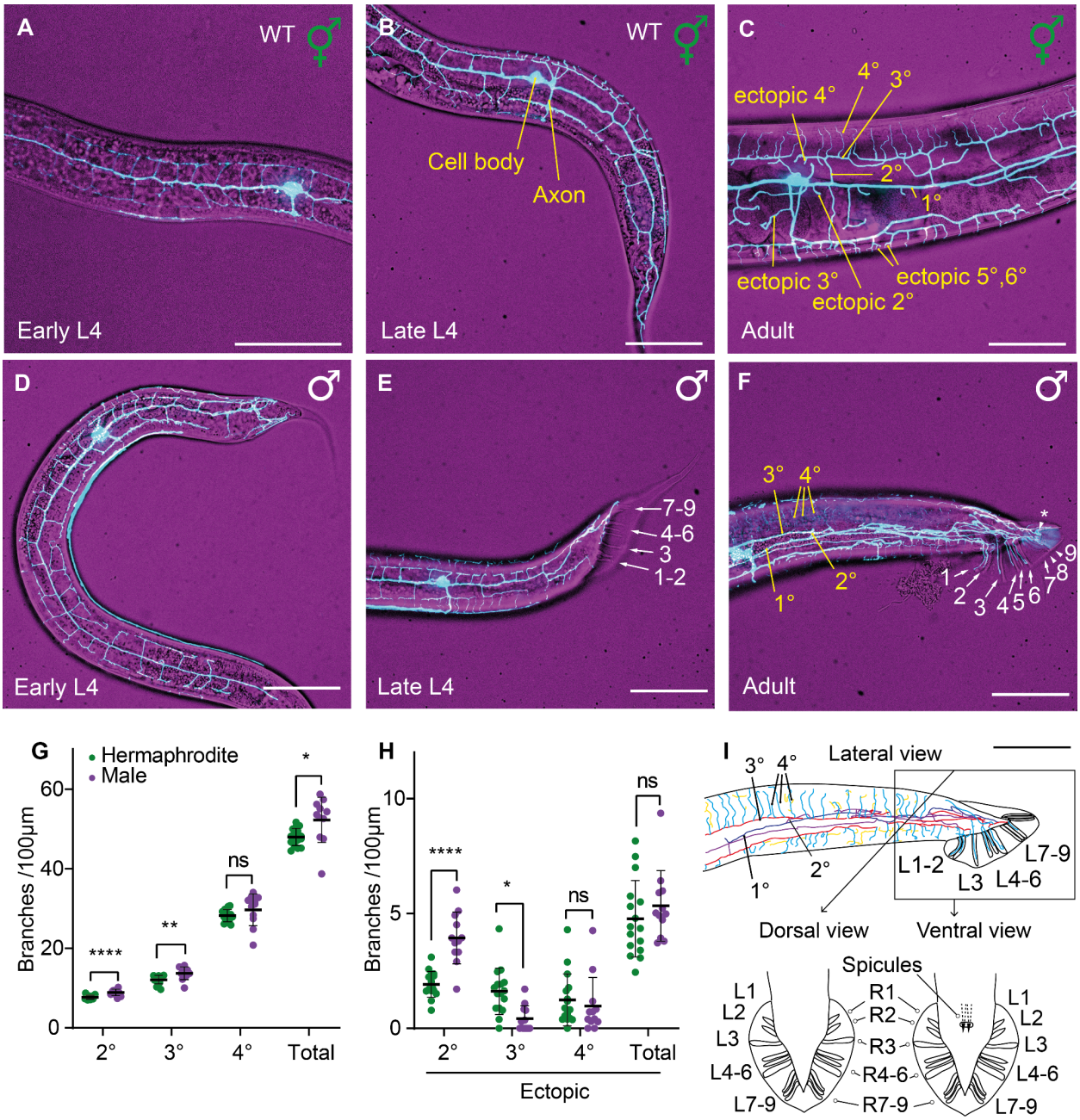

Figure 1 WT male PVD development shows post-larval sexual dimorphism

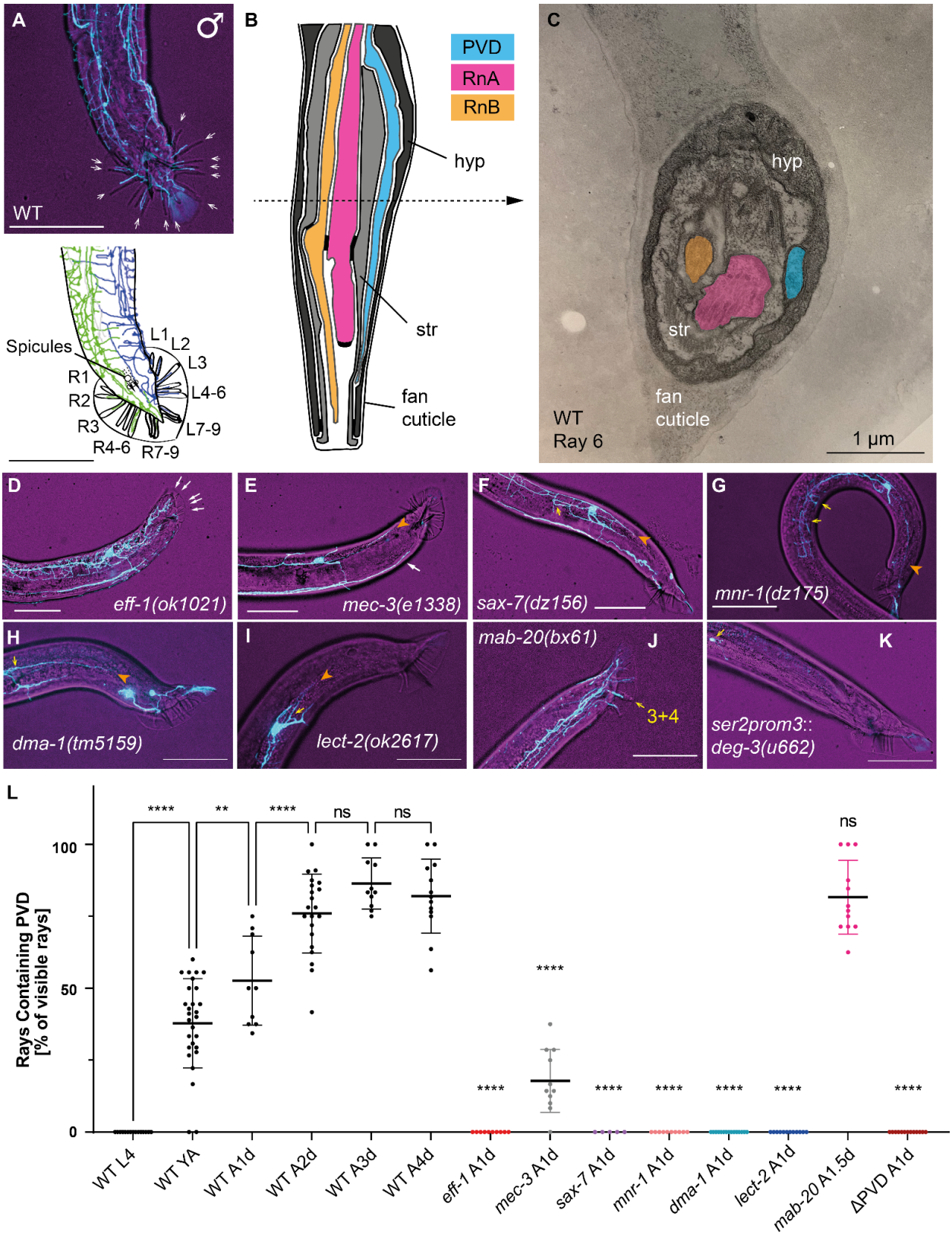

Figure 2 Mutants affecting hermaphrodite PVD morphology show similar male phenotypes

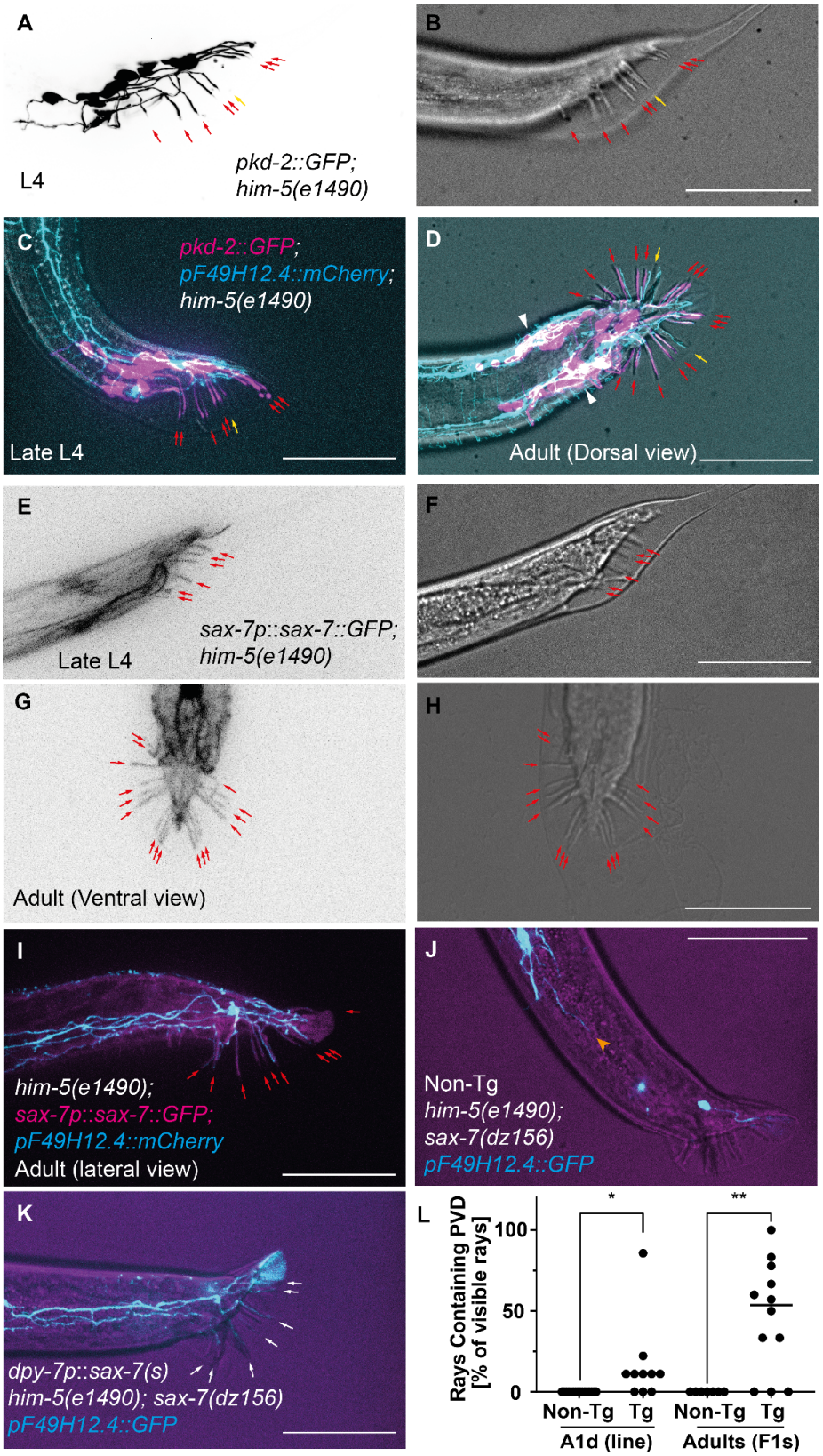

Figure 3 RnB neuron and *sax-7*::GFP signal appear in rays prior to PVD extension

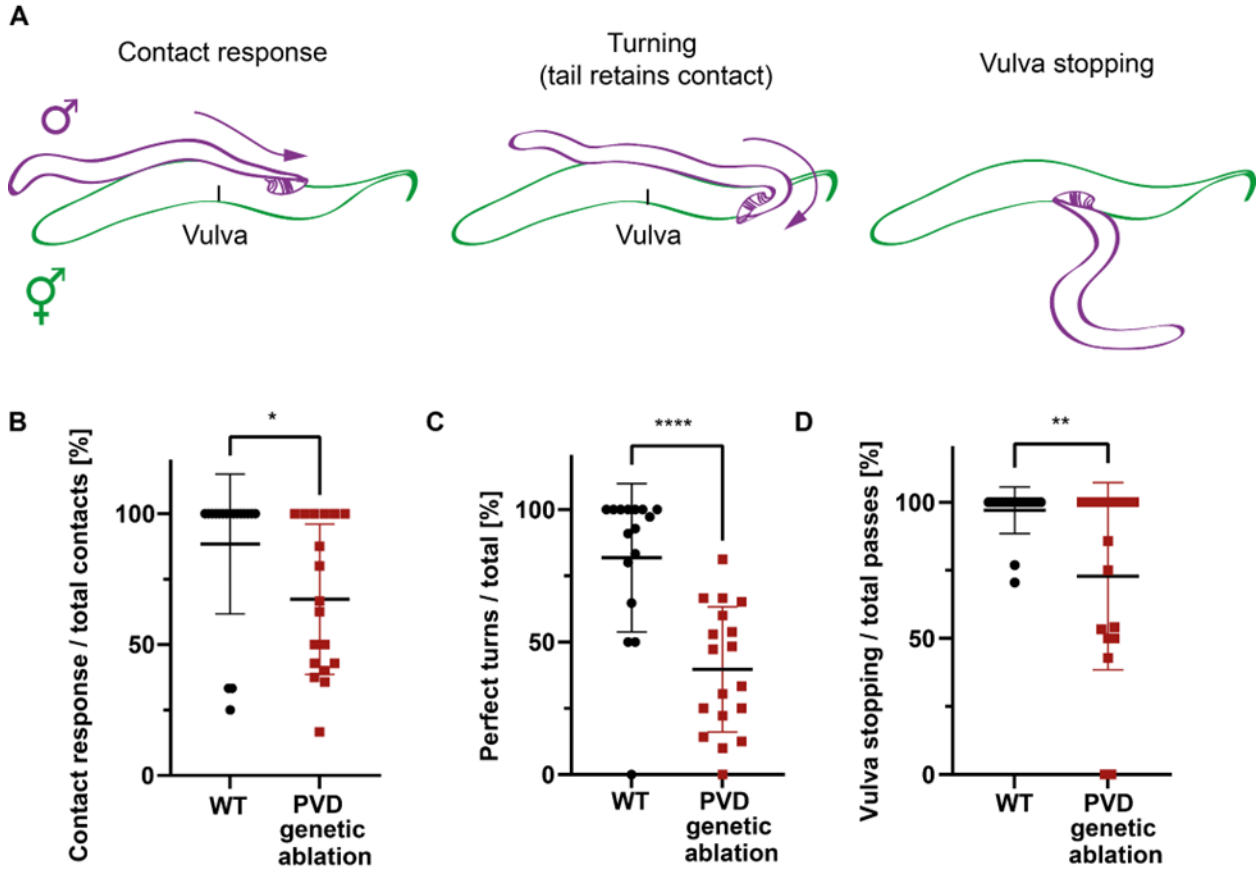

Figure 4 Mating behavior is impaired under PVD genetic ablation